FULL PAPER

MR texture analysis in differentiating renal cell carcinoma from lipid-poor angiomyolipoma and oncocytoma

[1]ABDUL RAZIK, [1]ANKUR GOYAL, [1]RAJU SHARMA, MD, [1]DEVASENATHIPATHY KANDASAMY, [2]AMLESH SETH, [3]PRASENJIT DAS and [4]BALAJI GANESHAN

[1]Departments of Radiology, All India Institute of Medical Sciences, Ansari Nagar, New Delhi, India
[2]Departments of Urology, All India Institute of Medical Sciences, Ansari Nagar, New Delhi, India
[3]Departments of Pathology, All India Institute of Medical Sciences, Ansari Nagar, New Delhi, India
[4]Institute of Nuclear Medicine, University College London Hospital NHS Trust, London, United Kingdom

Address correspondence to: Dr Raju Sharma
E-mail: *raju152@yahoo.com*

Objectives: To assess the utility of magnetic resonance texture analysis (MRTA) in differentiating renal cell carcinoma (RCC) from lipid-poor angiomyolipoma (lpAML) and oncocytoma.

Methods: After ethical approval, 42 patients with 54 masses (34 RCC, 14 lpAML and six oncocytomas) who underwent MRI on a 1.5 T scanner (Avanto, Siemens, Erlangen, Germany) between January 2011 and December 2012 were retrospectively included in the study. MRTA was performed on the TexRAD research software (Feedback Plc., Cambridge, UK) using free-hand polygonal region of interest (ROI) drawn on the maximum cross-sectional area of the tumor to generate six first-order statistical parameters. The Mann-Whitney U test was used to look for any statically significant difference. The receiver operating characteristic (ROC) curve analysis was done to select the parameter with the highest class separation capacity [area under the curve (AUC)] for each MRI sequence.

Results: Several texture parameters on MRI showed high-class separation capacity (AUC > 0.8) in differentiating RCC from lpAML and oncocytoma. The best performing parameter in differentiating RCC from lpAML was mean of positive pixels (MPP) at SSF 2 (AUC: 0.891) on DWI b500. In differentiating RCC from oncocytoma, the best parameter was mean at SSF 0 (AUC: 0.935) on DWI b1000.

Conclusions: MRTA could potentially serve as a useful non-invasive tool for differentiating RCC from lpAML and oncocytoma.

Advances in knowledge: There is limited literature addressing the role of MRTA in differentiating RCC from lpAML and oncocytoma. Our study demonstrated several texture parameters which were useful in this regard.

INTRODUCTION

Angiomyolipoma (AML) and oncocytoma are the most common benign renal neoplasms. In a study which analyzed the final histopathological diagnosis of 916 patients who underwent partial nephrectomy for a presumptive imaging diagnosis of renal cell carcinoma (RCC), 129 had benign disease, of which oncocytoma (51.2 %) and AML (28.7%) were the most prevalent entities.[1]

Oncocytomas and AML have better prognosis and different treatment strategies than RCC. AMLs are generally kept on observation unless they enlarge more than 4 cm, show rapid interval growth or bleed. In case of lipid-rich AML, the imaging diagnosis is often straightforward; however, lipid-poor AMLs (lpAML) are very difficult to differentiate from RCC. Several imaging findings may suggest the diagnosis of lpAML.[2,3] However, none of these are diagnostic or obviate the need for biopsy, which also carries a potential risk of hemorrhage.[4] Oncocytomas, on the other hand, are generally excised since a reliable distinction from RCC cannot be made even on biopsy. This is because hybrid tumors of oncocytoma and RCC (particularly, the chromophobe variant) are known to occur and any possible foci of RCC within the tumor may be undersampled on biopsy. Also, oncocytomas show a wide spectrum of imaging appearances attributable to varying proportions of cellular and stromal components and closely mimic RCC.[5,6] However, since imaging provides a holistic tool for non-invasively evaluating the entire tumor, any imaging modality capable of accurate differentiation between the two entities would

Figure 1. Flow diagram demonstrating how patients were enrolled in the study.
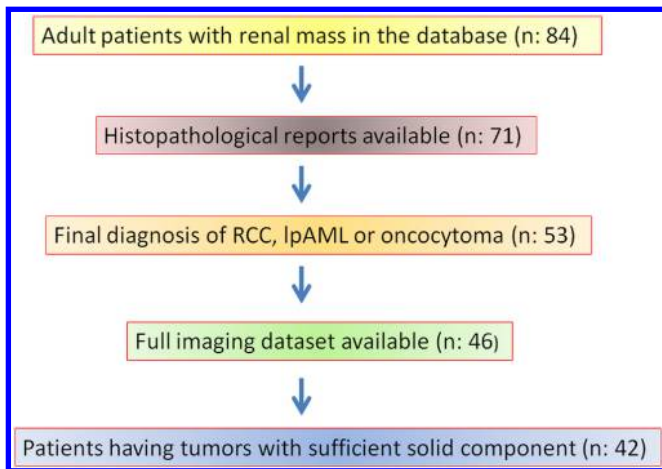
be extremely beneficial. The recent emergence of radiomics and texture analysis (TA) has introduced a new paradigm for the assessment of tumor characteristics. Radiomics uses pixel-level quantitative parameters which are not apparent to the human eye, potentially predicting microscopic necrosis and tumor aggressiveness.[7] Multiple studies have used TA to differentiate RCC from lpAML and oncocytoma on contrast-enhanced CT images.[8–23] MRI could potentially be superior to CT since it provides multiple paradigms for the morphological and functional assessment of renal tumors. With the increasing availability of scanners and heightened awareness of radiation safety, MRI is likely to be used increasingly in the future for assessment of renal tumors. However, the current literature on the role of magnetic resonance texture analysis

(MRTA) in differentiating benign and malignant renal lesions is scant. The only such study performed till date used texture analysis on diffusion-weighted imaging (DWI) to differentiate lpAML from clear cell RCC and observed that lpAML had significantly lower mean ADC and higher skewness than clear cell RCC.[24] Texture analysis was not applied to the other sequences. Hence, we attempted to better evaluate the role of MRTA in differentiating RCC from lpAML and oncocytoma.

METHODS AND MATERIALS

Patient selection

The MRI records of a previously ethically approved study conducted between January 2011 and December 2012 were retrospectively reviewed for adult patients with renal masses. Informed consent had already been taken from all the patients. The search yielded a consecutive sample of 84 patients. Among them, the follow-up histopathological report of the subsequently performed biopsy or nephrectomy specimen was available only in 71 patients. The patients who had histopathological diagnosis other than RCC, lpAML or oncocytoma (*n* = 18) were excluded from the study. Seven additional patients were excluded as their complete imaging dataset could not be retrieved from the picture archiving and communications system (PACS). Four patients were excluded since their tumors were primarily cystic and without sufficient solid components (at least 1 cm^2) for drawing a reasonably large region of interest (ROI). Thus, a total of 42 patients were included in the study. Among them, three patients had four lesions each, and another three had two lesions each. Finally, a total of 54 tumors underwent MRTA. The course of the patients enrolled in the study is demonstrated as a flow diagram (Figure 1).

Table 1. MRI sequences and acquisition parameters

Sequence	TR (ms)	TE (ms)	Slice thickness (mm)	Flip angle (degrees)	No. of averages	FOV (mm)	Matrix
T2W TSE FS Axial	2520	100	5	137	1	278 × 370	288 × 512
T2W TSE FS Coronal	2700	100	5	137	1	410 × 430	171 × 256
T1W GRE In-phase	125	4.76	5	70	1	278 × 370	288 × 512
T1W GRE Out-of-phase	125	2.34	5	70	1	278 × 370	288 × 512
True FISP Axial	3.4	1.4	5	39	1	263 × 350	288 × 512
True FISP Coronal	3.4	1.4	5	36	1	380 × 380	410 × 512
DWI FS Axial (b0, 500, 1000 s/ mm^2)	1600	62	7	90	6	249 × 380	94 × 192
T1W FS VIBE 3D (Axial)	5.1	2.3	3	10	1	253 × 450	158 × 512

DWI, Diffusion-weighted imaging; FISP, Fast imaging with steady state precession; FOV, Field of view; FS, Fat suppressed; GRE, Gradient-recalled echo; TE, Time to echo; TR: Time to repeat,TSE, Turbo spin echo; **T1W**: T_1-weighted, **T2W**: T_2-weighted;,VIBE, Volume interpolated breath-hold examination.

MRI acquisition parameters

A 1.5 T scanner (Avanto, Siemens, Erlangen, Germany) and a 16-channel-phased array torso coil were used. Non-contrast sequences included fat-suppressed T2W turbo spine-echo (T2W TSE) and T1W dual gradient-echo in-phase (TE: 4.76 ms) and out-of-phase (TE: 2.34 ms) images acquired over multiple breath-holds in the axial plane, true fast imaging with

Figure 2. Method of ROI placement on the post-contrast T1W image (nephrographic phase). (A) 36-year-old female with lpAML of the right kidney. ROI was drawn in the section showing the largest cross-sectional area of the tumor so as to include the entire tumor, except the peripheral 3 mm. (B) 61-year-old male with clear cell RCC of left kidney. The tumor shows multiple non-enhancing areas, suggestive of necrosis (*asterisk*). ROI was drawn in the section showing the largest dimension of the tumor, encompassing the largest non-necrotic zone.
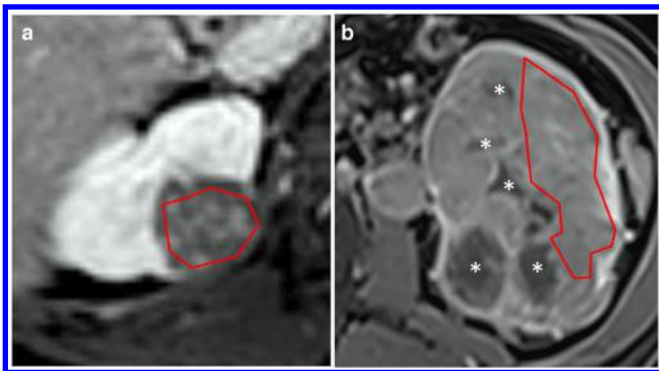

Figure 3. A 47-year-old female with oncocytoma of the left kidney. (A) ROI placement on the post-contrast T1W image in the nephrographic phase. The free-hand polygonal ROI (red contour) is drawn on the section containing the maximum cross-sectional area of the tumor, avoiding the peripheral 3 mm and any necrotic component. (B, C and D) Post-filtration texture analysis images at fine (B), medium (C) and coarse (D) spatial scaling factors.
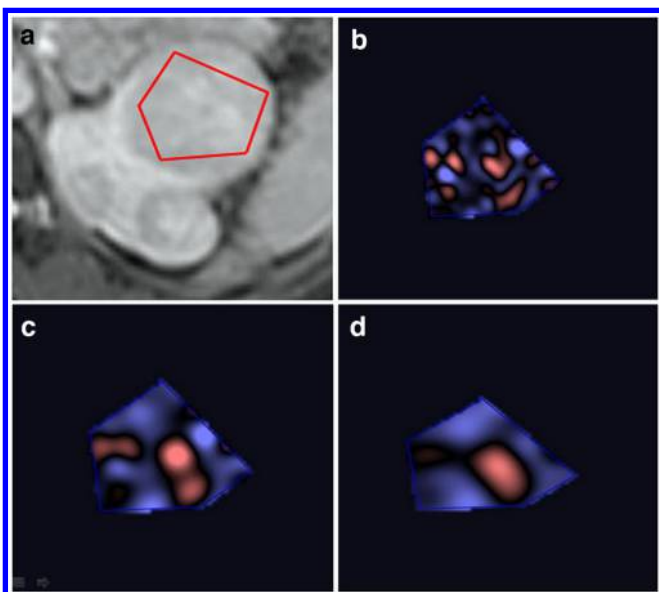
steady-state precession (TrueFISP) acquired in the axial and coronal planes in a single breath-hold and echo-planar imaging (EPI)-based DWI using navigator-triggered respiratory gating and diffusion-sensitizing gradients in all the three orthogonal planes (b values of 0, 500 and 1000 s/mm^2). After acquisition, a pixel-wise apparent diffusion coefficient (ADC) map was auto-generated using the b-values of 0 and 500 s/mm^2.

Post-contrast imaging was done using fat-suppressed 3D T1W volume interpolated breath-hold examination (VIBE) sequence in the axial plane after intravenous injection of gadobenate dimeglumine (Multihance, Bracco, Milan, Italy). For injection, the dual-head pressure injector was set at a rate of 2 ml s^{-1}, followed by a 20 ml saline bolus chase at the same rate. Bolus-tracking method was used to perform multiphase acquisition at 40–50 s [corticomedullary (CM) phase], 80–100 s [nephrographic (NG) phase] and 180 s (delayed phase). Post-contrast images were not available for 11 patients (15 tumors; 10 RCC and five lpAML). The imaging parameters are detailed in Table 1.

Feature extraction: MRTA

Texture analysis was performed on both the non-contrast and post-contrast images for 31 patients, whereas only the non-contrast images were assessed in the remaining 11 patients (15 tumors). A single radiologist (A.R., with 6 years of experience in diagnostic imaging), blinded to the final histopathological diagnosis, performed the TA. The axial dataset of the pre-contrast fat-suppressed T1-VIBE, T2W TSE images, DWI images at b500 and b1000 s/mm^2, ADC maps and the post-contrast CM and NG phase T1-VIBE images were uploaded onto the TexRAD software (Feedback Plc., Cambridge, UK-www.fbkmed.com). After screening the NG phase images to assess the distribution of the viable tumor component, a free-hand polygonal ROI (size: at least 1 cm^2) was drawn on all the above sequences in the slice showing the largest cross-sectional area of the tumor (Figure 2). The peripheral 3 mm of the tumor was avoided to prevent potential errors arising from inclusion of perirenal fat and volume averaging. Primarily cystic tumors without sufficient solid viable components of at least 1 cm^2 were excluded from the analysis. We excluded necrotic areas in the ROI to mitigate the confounding effect of macroscopic necrosis and enable the texture analysis results to truly reflect microscopic heterogeneity of the viable areas. Multiple ROIs and volume ROI were not used as they were cumbersome. In cases of multifocal disease with similar-appearing lesions, a maximum of two lesions per kidney were analyzed.

TexRAD software is based on the filtration-histogram technique, which uses a Laplacian of Gaussian spatial band-pass filter to enhance features corresponding to the size of the different spatial scaling factors (SSF) applied. The filtration step helps to mitigate the effects of photon noise on texture quantification. Five spatial scale filters (SSF) [2 mm (fine texture), 3, 4 and 5 mm (medium texture), and 6 mm (coarse texture)] were used apart from the unfiltered images (SSF: 0 mm) (Figure 3). The software then generated a pixel intensity distribution histogram and performed texture feature

Table 2. Mann-Whitney U test in the differentiation of RCC from lpAML: *P*-value of all the evaluated texture parameters, listed MR sequence-wise. Parameters showing statistical significance (*p* < 0.05) are highlighted in bold

SSF		SD	Entropy	MPP	Skewness	Kurtosis
T2W						
0	0.505	0.111	0.144	0.505	0.896	0.858
2	1.000	0.128	0.244	0.175	0.739	0.16
3	0.568	0.274	0.221	0.905	0.924	0.576
4	0.354	0.461	0.128	0.794	0.775	0.419
5	0.264	0.366	0.147	0.84	0.924	0.498
6	0.183	0.254	0.264	0.972	0.803	0.83
DWI b 500						
0	**0.003**	**0.01**	0.617	**0.003**	0.279	0.161
2	**0.000**	**0.000**	0.821	**0.000**	0.341	0.071
3	**0.001**	**0.000**	1.000	**0.000**	0.934	**0.017**
4	**0.001**	**0.000**	0.849	**0.000**	0.513	0.08
5	**0.001**	**0.001**	0.669	**0.001**	0.419	0.212
6	**0.002**	**0.001**	0.568	**0.002**	0.216	0.529
DWI b 1000						
0	**0.003**	**0.048**	0.757	**0.003**	**0.044**	0.877
2	**0.001**	**0.003**	0.419	**0.000**	0.924	**0.008**
3	**0.001**	**0.005**	0.341	**0.000**	0.821	**0.016**
4	**0.001**	**0.01**	0.521	**0.000**	0.544	0.091
5	**0.000**	**0.013**	0.703	**0.000**	0.335	0.405
6	**0.000**	**0.013**	0.877	**0.000**	0.072	0.953
ADC						
0	**0.001**	0.482	**0.015**	**0.001**	**0.010**	0.963
2	0.102	0.525	**0.033**	0.421	0.441	0.204
3	0.221	0.482	**0.029**	0.156	0.511	0.489
4	0.352	0.734	**0.035**	0.087	0.15	0.395
5	0.221	0.964	**0.032**	**0.022**	0.675	0.102
6	0.221	0.751	**0.036**	**0.013**	0.910	0.642
T1W						
0	**0.012**	**0.043**	1.000	**0.012**	0.149	0.301
2	**0.015**	**0.009**	0.116	**0.003**	0.612	0.528
3	**0.008**	**0.034**	0.233	**0.005**	0.396	0.177
4	**0.009**	**0.043**	0.469	**0.009**	0.379	0.132
5	**0.017**	**0.043**	0.528	**0.017**	0.124	0.21
6	**0.024**	0.072	0.548	**0.022**	0.102	0.346
Corticomedullary phase						
0	**0.017**	0.170	0.133	**0.017**	0.363	**0.027**
2	0.409	**0.022**	0.145	**0.047**	0.536	0.592
3	0.483	**0.031**	0.112	0.094	0.409	0.564
4	0.742	**0.047**	0.071	0.145	0.409	0.621

(Continued)

Table 2. (Continued)

| 5 | 0.902 | 0.122 | 0.064 | 0.341 | 0.386 | 0.433 |
6	0.934	0.122	0.064	0.086	0.509	0.773
Nephrographic phase						
0	0.079	0.179	0.121	0.079	0.564	0.890
2	0.154	**0.036**	0.072	0.102	0.827	0.592
3	0.238	0.059	**0.040**	0.222	0.619	0.309
4	0.254	0.179	**0.040**	0.619	0.827	**0.044**
5	0.309	0.238	**0.040**	0.796	0.766	**0.020**
6	0.392	0.207	**0.049**	0.890	0.984	0.086

extraction to derive six quantitative first-order statistical metrics at each SSF: mean, standard deviation (SD), entropy, mean of positive pixels (MPP), skewness and kurtosis. Thus, 36 texture variables were generated for each lesion.

Statistical analysis

The IBM SPSS software for Windows, v.24.0 (IBM Corp, Armonk, NY, USA) was used to perform statistical analysis. To compare the differences in texture parameters between RCC and lpAML, as well as RCC and oncocytoma, the non-parametric Mann-Whitney U test was used. A *p*-value $\leq$ 0.05 was considered significant.

As the first step in differentiating RCC *vs* lpAML and RCC *vs* oncocytoma, all the parameters with statistical significance (*p*-value $\leq$ 0.05) were listed. Subsequently, all the significant parameters underwent receiver operating characteristic (ROC) curve analysis to generate the area under curve (AUC) and optimal cut-off value. All parameters with AUC greater than or equal to 0.8 were highlighted and the parameter with the highest AUC value was selected as the best performing metric

Figure 4. Box and whisker representation of the best-performing parameter in differentiating RCC from lpAML (MPP at SSF two on DWI b500). The Y-axis represents the MPP of the signal intensity values.
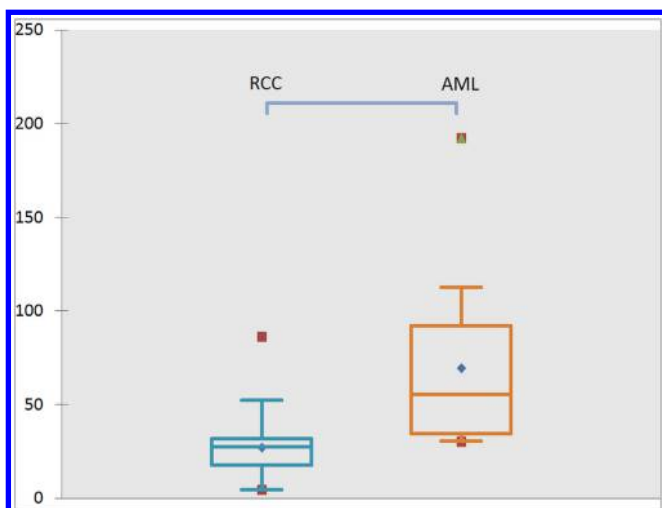
for each sequence. In case a tie occurred for the same texture parameter at multiple SSFs, the metric at the highest SSF was selected since higher SSF is known to mitigate photon noise and provide more accurate parameters than the lower filters. In case a tie occurred between two different texture parameters, the Pearson's correlation test would be applied to look for mutual correlation. In case a strong mutual correlation (*r* > 0.9) was observed, only one of the parameters was retained to remove redundancy. This issue occurred mostly with ADC since it contains only positive pixels and hence generates similar mean and MPP values. In such cases, by default, only mean was retained.

RESULTS

The mean age of the study population (42 patients) was 43.6 years and a male predominance (27 males *vs* 15 females) was observed. The population had a total of 34 RCCs (33 patients; 29 clear cell RCC, four papillary RCC and one chromophobe RCC), 14 lpAML (six patients) and six oncocytomas (three patients). One patient with clear cell RCC had two lesions. The results of MRTA in differentiating the subtypes and grades of RCC from the same dataset have already been published.[25] Among patients with lpAML, two patients had four lesions each, two had two lesions each and the remaining two had one lesion each. In the oncocytoma group, one patient had four lesions and two patients had one lesion each. Among RCCs, the majority of patients were males (27 males *vs* 7 females). On the other hand, all the patients with lpAML were females. In the Oncocytoma cohort, one patient was male and two were females. The overall mean tumor diameter was 5.93 $\pm$ 2.8 cm and the mean ROI size was 2.4 $\pm$ 0.7 cm^2. The mean tumor diameter was 7.54 $\pm$ 1.89 cm, 2.79 $\pm$ 1.19 cm and 2.97 $\pm$ 0.68 cm for RCC, lpAML and oncocytomas, respectively. The mean ROI size was 2.36 $\pm$ 0.72 cm^2, 2.42 $\pm$ 0.59 cm^2 and 2.28 $\pm$ 0.39 cm^2 for RCC, lpAML and oncocytomas, respectively.

Differentiation of RCC from lpAML

A total of 82 metrics across all the sequences (none on T2W imaging, 19 on DWI b500, 21 on DWI b1000, 11 on the ADC map, 17 on the unenhanced T1W image, and seven each on the postcontrast CM and NG Phase images) showed statistical significance in differentiating RCC from lpAML (Table 2).

Table 3. AUC values and diagnostic performance of all the parameters which showed statistical significance ($p < 0.05$) in the differentiation of RCC from lpAML, listed MR sequence-wise. The sequence-wise single best parameters are highlighted with asterisk

Parameter	SSF	AUC	Cut-off	Sensitivity	Specificity	PPV	NPV	Accuracy
T2W								
DWI b500								
Mean	0	0.781	≤194.730	85.3	61.5	85.3	61.5	78.7
Mean	2	0.833	≤11.370	79.4	76.9	90.0	58.8	78.7
Mean	3	0.828	≤29.530	79.4	76.9	90.0	58.8	78.7
Mean	4	0.810	≤44.480	76.5	76.9	89.7	55.6	76.6
Mean	5	0.803	≤41.290	61.8	92.3	95.5	48.0	70.2
Mean	6	0.790	≤51.680	58.8	92.3	95.2	46.2	68.1
SD	0	0.747	≤15.460	79.4	61.5	84.4	53.3	74.5
SD	2	0.855	≤37.760	76.5	84.6	92.9	57.9	78.7
SD	3	0.867	≤48.040	79.4	84.6	93.1	61.1	80.9
SD	4	0.851	≤51.050	70.6	92.3	96.0	54.5	76.6
SD	5	0.826	≤51.460	70.6	92.3	96.0	54.5	76.6
SD	6	0.808	≤58.030	79.4	76.9	90.0	58.8	78.7
MPP	0	0.781	≤194.730	85.3	61.5	85.3	61.5	78.7
MPP	2	0.891*	≤30.510	70.6	100.0	100.0	56.5	78.7
MPP	3	0.867	≤42.610	73.5	84.6	92.6	55.0	76.6
MPP	4	0.846	≤64.150	76.5	84.6	92.9	57.9	78.7
MPP	5	0.821	≤55.670	61.8	92.3	95.5	48.0	70.2
MPP	6	0.792	≤77.870	67.6	84.6	92.0	50.0	72.3
Kurtosis	3	0.726	≥0.270	47.1	100.0	100.0	41.9	61.7
DWI b1000								
Mean	0	0.778	≤71.660	55.9	92.3	95.0	44.4	66.0
Mean	2	0.824	≤8.830	85.3	84.6	93.5	68.8	85.1
Mean	3	0.828	≤16.400	85.3	84.6	93.5	68.8	85.1
Mean	4	0.821	≤22.290	79.4	84.6	93.1	61.1	80.9
Mean	5	0.835	≤30.780	79.4	84.6	93.1	61.1	80.9
Mean	6	0.855	≤40.750	79.4	84.6	93.1	61.1	80.9
SD	0	0.688	≤14.500	91.2	46.2	81.6	66.7	78.7
SD	2	0.778	≤20.140	52.9	92.3	94.7	42.9	63.8
SD	3	0.765	≤41.590	88.2	53.8	83.3	63.6	78.7
SD	4	0.747	≤33.170	76.5	61.5	83.9	50.0	72.3
SD	5	0.735	≤37.700	79.4	61.5	84.4	53.3	74.5
SD	6	0.738	≤34.700	76.5	76.9	89.7	55.6	76.6
MPP	0	0.778	≤71.660	55.9	92.3	95.0	44.4	66.0
MPP	2	0.839	≤21.100	76.5	76.9	89.7	55.6	76.6
MPP	3	0.839	≤26.640	70.6	92.3	96.0	54.5	76.6
MPP	4	0.833	≤29.560	67.6	92.3	95.8	52.2	74.5
MPP	5	0.860*	≤37.420	70.6	92.3	96.0	54.5	76.6

(Continued)

Table 3. (Continued)

Parameter	SSF	AUC	Cut-off	Sensitivity	Specificity	PPV	NPV	Accuracy
MPP	6	0.860	≤30.210	64.7	100.0	100.0	52.0	74.5
Skewness	0	0.691	≥−0.090	64.7	69.2	84.6	42.9	66.0
Kurtosis	2	0.753	≥−0.280	82.4	69.2	87.5	60.0	78.7
Kurtosis	3	0.730	≥−0.340	85.3	61.5	85.3	61.5	78.7
ADC								
Mean	0	0.800*	≥1302.82	73.5	92.9	96.2	59.1	79.2
Entropy	0	0.725	≥4.250	70.6	71.4	85.7	50.0	70.8
Entropy	2	0.697	≥3.870	88.2	50.0	81.1	63.6	77.1
Entropy	3	0.702	≥3.950	85.3	50.0	80.6	58.3	75.0
Entropy	4	0.695	≥3.950	85.3	50.0	80.6	58.3	75.0
Entropy	5	0.699	≥3.920	85.3	50.0	80.6	58.3	75.0
Entropy	6	0.694	≥3.950	85.3	50.0	80.6	58.3	75.0
MPP	0	0.800	≥1302.82	73.5	92.9	96.2	59.1	79.2
MPP	5	0.712	≥302.090	82.4	64.3	84.8	60.0	77.1
MPP	6	0.730	≥291.180	76.5	64.3	83.9	52.9	72.9
Skewness	0	0.738	≤0.270	69.7	78.6	88.5	52.4	72.3
T1W								
Mean	0	0.760	≤157.430	42.9	100.0	100.0	40.7	59.0
Mean	2	0.750	≤0.880	64.3	81.8	90.0	47.4	69.2
Mean	3	0.773	≤8.300	75.0	72.7	87.5	53.3	74.4
Mean	4	0.766	≤14.390	75.0	81.8	91.3	56.3	76.9
Mean	5	0.747	≤18.040	67.9	81.8	90.5	50.0	71.8
Mean	6	0.734	≤31.400	67.9	81.8	90.5	50.0	71.8
SD	0	0.711	≤12.540	64.3	81.8	90.0	47.4	69.2
SD	2	0.769	≤32.760	64.3	81.8	90.0	47.4	69.2
SD	3	0.721	≤67.470	85.7	54.5	82.8	60.0	76.9
SD	4	0.711	≤78.450	78.6	54.5	81.5	50.0	71.8
SD	5	0.711	≤98.730	89.3	45.5	80.6	62.5	76.9
MPP	0	0.760	157.430	42.9	100.0	100.0	40.7	59.0
MPP	2	0.805*	29.560	64.3	81.8	90.0	47.4	69.2
MPP	3	0.786	70.430	89.3	54.5	83.3	66.7	79.5
MPP	4	0.766	33.270	42.9	100.0	100.0	40.7	59.0
MPP	5	0.747	34.210	39.3	100.0	100.0	39.3	56.4
MPP	6	0.737	50.110	50.0	90.9	93.3	41.7	61.5
Corticomedullary phase								
Mean	0	0.773	≤431.530	78.3	77.8	90.0	58.3	78.1
SD	2	0.763	≤92.010	69.6	77.8	88.9	50.0	71.9
SD	3	0.749	≤128.970	73.9	66.7	85.0	50.0	71.9
SD	4	0.729	≤102.580	47.8	100.0	100.0	42.9	62.5

(Continued)

Table 3. (Continued)

Parameter	SSF	AUC	Cut-off	Sensitivity	Specificity	PPV	NPV	Accuracy
MPP	0	0.773	≤431.530	78.3	77.8	90.0	58.3	78.1
MPP	2	0.729	≤60.900	47.8	88.9	91.7	40.0	59.4
Kurtosis	0	0.751	≤−0.410	52.2	88.9	92.3	42.1	62.5
Nephrographic phase								
SD	2	0.741	≤106.180	75.0	66.7	85.7	50.0	72.7
Entropy	3	0.736	≥5.180	75.0	77.8	90.0	53.8	75.8
Entropy	4	0.734	≥5.190	79.2	66.7	86.4	54.5	75.8
Entropy	5	0.734	≥5.230	79.2	66.7	86.4	54.5	75.8
Entropy	6	0.727	≥5.150	79.2	66.7	86.4	54.5	75.8
Kurtosis	4	0.729	≥−0.080	62.5	88.9	93.8	47.1	69.7
Kurtosis	5	0.764	≥−0.150	62.5	88.9	93.8	47.1	69.7

Subsequently, the AUC values of all the significant parameters were listed (Table 3). The following were the sequence-wise best parameters (highest AUC) in differentiating RCC from lpAML: (a) MPP at SSF 2 (AUC: 0.891) on DWI b500 (b) MPP at SSF 5 (AUC: 0.860) on DWI b1000 (c) mean at SSF 0 (AUC: 0.800) on the ADC map and (d) MPP at SSF 2 (AUC: 0.805) on the T1W images (Table 4). On the ADC images, both mean and MPP at SSF 0 showed strong correlation ($r = 1.0$), which was expected since ADC maps possess only positive pixels. Hence only the mean was retained. On the CM and NG phase images, none of the parameters were observed to have high-class separation capacity (AUC > 0.8). The optimal cut-off values are shown in Table 3. The box and whisker plot of the single best forming parameter (MPP at SSF two on DWI b500) is given in Figure 4.

Differentiation of RCC from oncocytoma
The *p*-values of all the parameters derived from the Mann-Whitney analysis were tabulated separately for each MR sequence and the metrics with significant *p*-value were identified (Table 5). This yielded a total of 107 metrics across all the sequences (15 on T2W imaging, 18 each on DWI b500 and b1000, 17 on the ADC map, 11 on the unenhanced T1W images, 18 on the postcontrast CM phase images and 10 on the NG phase images).

Subsequently, AUC values of all parameters which showed significant *p*-value were listed and the parameters with the

Table 4. Sequence-wise best-performing parameters (having AUC of at least 0.8) in the differentiation of RCC from lpAML (No parameter qualified for remaining sequences)

Sequence	Parameter	SSF value	AUC
DWI b500	MPP	2	0.891
DWI b1000	MPP	5	0.860
ADC map	Mean	0	0.800
T1W	MPP	2	0.805

highest AUC were identified (Table 6). The following were the sequence-wise best parameters in differentiating RCC from oncocytoma: (a) MPP at SSF 6 (AUC: 814) on T2W images (b) MPP at SSF 6 (AUC: 0.931) on DWI b500 (c) mean at SSF 0 (AUC: 0.935) on DWI b1000 (d) SD at SSF 0 (AUC: 0.875) on the ADC map, (e) MPP at SSF 2 (AUC: 0.875) on T1W images, (f) mean at SSF 0 (AUC: 913) on the CM phase images and (g) mean at SSF 0 (AUC: 868) on the NG phase images (Table 7). On the DWI b1000, CM and NG phase images, both mean and MPP at SSF 0 showed strong correlation ($r = 1.0$), which possibly occurred since all the three image sets contained only positive pixels. Hence, only the mean was retained. The optimal cut-off values are listed in Table 6. The box and whisker plot of the single best-forming parameter (mean at SSF 0 on DWI b1000) is given in Figure 5.

DISCUSSION
The risks of hemorrhage in lpAML and potentially missing a hybrid RCC in oncocytomas are inherent with biopsy.[4,5] There is an active ongoing search for imaging biomarkers which can differentiate RCC from lpAML and oncocytoma. Radiomics is one such novel tool which has been found to be useful for this purpose.

Texture analysis quantifies pixel-level heterogeneity in the grayscale within the selected ROI. Among the six first-order parameters generated, mean and MPP quantify overall grayscale intensity and show greater values with higher signal intensity and enhancement. SD and entropy quantify dispersion and disorder respectively, and show positive correlation with increasing heterogeneity. Skewness is a measure of the asymmetry of the histogram, with positive skewness representing a decrease in the number of brighter pixels and vice versa. Kurtosis measures the peakedness of the histogram, and shows lower values with increasing heterogeneity.[26] In our study, several texture parameters showed good diagnostic performance in differentiating RCC from lpAML and oncocytoma.

Table 5. Mann-Whitney U test in the differentiation of RCC from oncocytoma: *P*-value of all the evaluated texture parameters, listed MR sequence-wise. Parameters showing statistical significance ($p < 0.05$) are highlighted in bold

SSF	Mean	SD	Entropy	MPP	Skewnes	Kurtosis
T2W						
0	**0.037**	0.109	0.517	**0.037**	**0.033**	0.383
2	0.171	0.225	0.493	0.148	0.566	0.288
3	0.078	0.109	0.517	0.137	**0.03**	0.868
4	**0.041**	**0.019**	0.383	**0.041**	**0.021**	1.000
5	**0.037**	**0.017**	0.404	**0.027**	**0.017**	0.698
6	**0.033**	**0.015**	0.324	**0.013**	0.137	0.926
DWI b 500						
0	**0.001**	0.06	0.592	**0.001**	0.839	0.343
2	**0.002**	**0.001**	0.071	**0.000**	**0.045**	0.566
3	**0.003**	**0.000**	0.092	**0.000**	0.078	1.000
4	**0.002**	**0.000**	0.109	**0.000**	0.197	0.839
5	**0.001**	**0.000**	0.127	**0.000**	0.118	0.868
6	**0.001**	**0.001**	0.137	**0.000**	0.306	0.956
DWI b 1000						
0	**0.001**	**0.009**	0.334	**0.001**	0.474	0.474
2	**0.005**	**0.007**	0.192	**0.003**	0.334	0.823
3	**0.002**	**0.007**	0.207	**0.002**	0.257	0.823
4	**0.002**	**0.008**	0.239	**0.002**	0.139	0.5
5	**0.002**	**0.009**	0.257	**0.001**	0.275	0.449
6	**0.003**	**0.011**	0.356	**0.002**	0.526	0.449
ADC						
0	**0.007**	**0.002**	**0.004**	**0.007**	0.872	0.442
2	0.897	0.127	**0.006**	**0.027**	0.644	**0.013**
3	0.897	0.159	**0.006**	**0.017**	0.839	**0.033**
4	0.493	0.159	**0.006**	**0.017**	0.240	0.425
5	0.566	0.118	**0.004**	**0.012**	0.148	**0.003**
6	0.541	0.092	**0.004**	**0.024**	0.071	0.644
T1W						
0	**0.017**	**0.047**	0.612	**0.017**	0.878	0.676
2	0.364	**0.005**	0.494	**0.003**	0.204	0.947
3	0.522	**0.011**	0.708	**0.029**	0.551	0.466
4	0.676	0.053	0.912	0.082	0.676	0.843
5	0.551	**0.042**	0.982	**0.047**	0.775	0.466
6	0.551	**0.033**	0.878	**0.026**	0.947	0.644
Corticomedullary phase						
0	**0.001**	0.192	0.581	**0.001**	0.618	0.445
2	0.174	**0.009**	0.142	**0.011**	**0.014**	**0.047**
3	0.062	**0.005**	0.102	**0.005**	**0.005**	0.174
4	**0.019**	**0.005**	0.158	**0.004**	0.054	0.773

(Continued)

Table 5. (Continued)

5	**0.014**	**0.004**	0.192	**0.004**	0.581	1.000
6	**0.008**	**0.009**	0.174	**0.003**	0.854	0.546
Nephrographic phase						
0	**0.004**	0.116	0.631	**0.004**	0.94	0.296
2	0.347	**0.021**	0.210	**0.044**	0.781	0.374
3	0.143	**0.038**	0.116	0.057	0.462	0.900
4	0.065	**0.025**	**0.104**	**0.044**	0.432	0.631
5	0.05	**0.018**	0.129	0.05	0.374	0.595
6	**0.038**	**0.044**	0.158	0.073	0.527	0.743

RCCs showed lesser diffusion restriction compared to lpAML, as indicated by the lower mean/ MPP values on the DWI b500/b1000 images and higher mean/MPP values on the ADC images. The SD values were also lower for RCC, suggesting a more homogeneous pattern of diffusion restriction. In the existing literature, DWI has shown variable results in the differentiation of RCC from lpAML with some studies showing greater diffusion restriction for RCC and vice versa.[27–30] This has been attributed to the variable composition of AML, with the lesions showing lesser amount of fat and greater proportion of myomatous content showing greater diffusion restriction and lower ADC values.[31] In addition, the presence of necrosis in RCC may result in increased diffusion and higher net ADC values. Li et al, in the only other study which used MRTA in the differentiation of RCC from lpAML, also observed lower mean ADC in lpAML than RCC.[24] However, their finding of a significantly higher skewness value in lpAML was not reproduced in our study. Our observation of a more homogeneous pattern of diffusion restriction in RCC contradicts the common logic and existing literature since RCC with the intrinsically higher propensity to undergo hemorrhage and necrosis is expected

Figure 5. Box and whisker representation of the best-performing parameter in differentiating RCC from oncocytoma (mean at SSF 0 on DWI b1000). The Y-axis represents the mean of the signal intensity values.
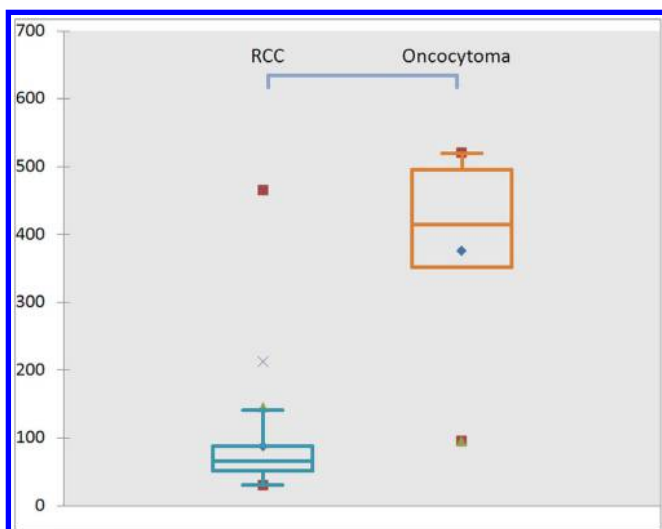
to show more heterogeneous diffusion restriction than lpAML which demonstrates more compact cellular arrangement.[32] On the unenhanced T1W images of our study, RCC showed lower mean/ MPP and SD values, suggestive of a lower and more homogeneous T1 signal in comparison with lpAML. This could be attributed to the greater proportion of pixel-level fat not appreciable to the naked eye in AML. In agreement with our study, Sasiwimonphan et al had also observed a higher T1 SI ratio for lpAML than RCC.[33] The level of corticomedullary phase enhancement was also lower and more homogeneous for RCC than lpAML in our study. The literature supports this finding since some studies have observed more intense early enhancement in lpAML than RCC, a feature attributed to the higher proportion of angiomatous components.[33,34] On the NG phase images, RCC showed higher entropy values than lpAML, suggestive of higher degree of randomness in the enhancement pattern.

In differentiating RCC from oncocytoma, T2W images showed significantly lower T2 signal intensity (mean/ MPP values) and more homogeneous pattern of T2 signal (lower SD) in RCC. Studies comparing oncocytoma and chromophobe RCC have observed higher and more heterogeneous T2 signal for oncocytomas, although this difference was not always significant.[6,35] In our study, RCC showed lower levels of diffusion restriction than oncocytoma as indicated by the lower mean/MPP values on the DWI b500/b1000 images and higher mean/ MPP values on the ADC images. Lower SD values on the DWI images also suggest a more homogeneous pattern of diffusion restriction in RCC. These findings are in contradiction with several studies which have observed that RCCs show higher diffusion restriction than oncocytoma.[29,36] However, in a study which included a clear cell RCC dominant cohort, Hötker et al observed that RCC showed lower diffusion restriction than oncocytoma.[37] He attributed the difference in the observation to the predominance of non-clear cell RCC in the other studies. Clear cell RCC is known to show much higher extent of necrosis and angiogenesis, all of which increases free diffusion. This also would explain the findings observed in our study, which had a predominance of clear cell RCC. RCC also showed lower and more homogeneous unenhanced T1 signal, corticomedullary and nephrographical phase enhancement than oncocytoma. In the literature, the enhancement pattern of oncocytomas has been extremely variable and

Table 6. AUC values and diagnostic performance of all the parameters which showed statistical significance (*p* < 0.05) in the differentiation of RCC from oncocytoma, listed MR sequence-wise. The sequence-wise single best parameters are highlighted with asterisk

Parameter	SSF	AUC	Cut-off	Sensitivity	Specificity	PPV	NPV	Accuracy
T2W								
Mean	0	0.77	≤398.840	97.1	66.7	94.3	80.0	92.5
Mean	4	0.765	≤21.670	50.0	100.0	100.0	26.1	57.5
Mean	5	0.77	≤38.390	50.0	100.0	100.0	26.1	57.5
Mean	6	0.775	≤189.060	85.3	66.7	93.5	44.4	82.5
SD	4	0.799	≤106.040	76.5	83.3	96.3	38.5	77.5
SD	5	0.804	≤114.030	73.5	83.3	96.2	35.7	75
SD	6	0.809	≤105.680	64.7	83.3	95.7	29.4	67.5
MPP	0	0.77	≤398.840	97.1	66.7	94.3	80	92.5
MPP	4	0.765	≤152.540	79.4	66.7	93.1	36.4	77.5
MPP	5	0.784	≤177.940	85.3	66.7	93.5	44.4	82.5
MPP	6	0.814*	≤212.970	85.3	66.7	93.5	44.4	82.5
Skewness	0	0.775	≤0.070	58.8	100.0	100.0	30.0	65.0
Skewness	3	0.777	≤0.380	76.5	83.3	96.3	38.5	77.5
Skewness	4	0.794	≤0.130	55.9	100.0	100.0	28.6	62.5
Skewness	5	0.804	≤0.350	70.6	83.3	96.0	33.3	72.5
DWI b500								
Mean	0	0.897	≤183.320	82.4	83.3	96.6	45.5	82.5
Mean	2	0.877	≤7.760	67.6	100.0	100.0	35.3	72.5
Mean	3	0.868	≤17.540	61.8	100.0	100.0	31.6	67.5
Mean	4	0.873	≤36.250	64.7	100.0	100.0	33.3	70
Mean	5	0.892	≤62.930	76.5	100.0	100.0	42.9	80
Mean	6	0.907	≤84.190	76.5	100.0	100.0	42.5	80
SD	2	0.907	≤33.910	70.6	100.0	100.0	37.5	75
SD	3	0.922	≤45.190	70.6	100.0	100.0	37.5	75
SD	4	0.926	≤64.440	91.2	83.3	96.9	62.5	90
SD	5	0.917	≤75.150	91.2	83.3	96.9	62.5	90
SD	6	0.892	≤79.940	91.2	83.3	96.9	62.5	90
MPP	0	0.897	≤183.320	82.4	83.3	96.6	45.5	82.5
MPP	2	0.919	≤32.060	76.5	100.0	100.0	42.9	80
MPP	3	0.922	≤48.040	76.5	100.0	100.0	42.9	80
MPP	4	0.922	≤68.180	79.4	100.0	100.0	46.2	82.5
MPP	5	0.922	≤85.990	79.4	100.0	100.0	46.2	82.5
MPP	6	0.931*	≤103.600	79.4	100.0	100.0	46.2	82.5
Skewness	2	0.76	≤0.530	82.4	83.3	96.6	45.5	82.5
DWI b1000								
Mean	0	0.935*	≤212.40	97.1	80.0	97.1	80.0	94.9
Mean	2	0.876	≤5.420	73.5	100.0	100.0	35.7	76.9
Mean	3	0.9	≤12.300	76.5	100.0	100.0	38.5	79.5
Mean	4	0.9	≤22.290	79.4	100.0	100.0	41.7	82.1

(Continued)

Table 6. (Continued)

Mean	5	0.906	≤30.780	79.4	100.0	100.0	41.7	82.1
Mean	6	0.894	≤38.640	76.5	100.0	100.0	38.5	79.5
SD	0	0.85	≤18.470	97.1	80.0	97.1	80.0	94.9
SD	2	0.865	≤54.680	97.1	80.0	97.1	80.0	94.9
SD	3	0.865	≤65.470	97.1	80.0	97.1	80.0	94.9
SD	4	0.859	≤66.270	97.1	80.0	97.1	80.0	94.9
SD	5	0.853	≤75.720	97.1	80.0	97.1	80.0	94.9
SD	6	0.847	≤78.180	97.1	80.0	97.1	80.0	94.9
MPP	0	0.935	≤212.40	97.1	80.0	97.1	80.0	94.9
MPP	2	0.888	≤44.140	94.1	80.0	97	66.7	92.3
MPP	3	0.906	≤57.100	94.1	80.0	97	66.7	92.3
MPP	4	0.900	≤57.810	91.2	80.0	96.9	57.1	89.7
MPP	5	0.912	≤73.170	91.2	80.0	96.9	57.1	89.7
MPP	6	0.900	≤85.050	91.2	80.0	96.9	57.1	89.7
ADC								
Mean	0	0.838	≥549.310	97.1	66.7	94.3	80.0	92.5
SD	0	0.875*	≥107.200	85.3	83.3	96.7	50	85.0
Entropy	0	0.85	≥2.710	97.1	66.7	94.3	80.0	92.5
Entropy	2	0.841	≥2.710	97.1	66.7	94.3	80.0	92.5
Entropy	3	0.843	≥2.710	97.1	66.7	94.3	80.0	92.5
Entropy	4	0.843	≥2.710	97.1	66.7	94.3	80.0	92.5
Entropy	5	0.858	≥2.710	97.1	66.7	94.3	80.0	92.5
Entropy	6	0.853	≥2.710	97.1	66.7	94.3	80.0	92.5
MPP	0	0.838	≥549.310	97.1	66.7	94.3	80.0	92.5
MPP	2	0.782	≥173.870	97.1	66.7	94.3	80.0	92.5
MPP	3	0.801	≥237.390	91.2	83.3	96.9	62.5	90.0
MPP	4	0.804	≥241.360	91.2	83.3	96.9	62.5	90.0
MPP	5	0.816	≥177.210	97.1	83.3	97.1	83.3	95
MPP	6	0.787	≥131.900	97.1	66.7	94.3	80.0	92.5
Kurtosis	2	0.814	≥−0.940	97.1	66.7	94.3	80.0	92.5
Kurtosis	3	0.772	≥−0.610	94.1	66.7	94.1	66.7	90.0
Kurtosis	5	0.86	≥−0.530	76.5	83.3	96.3	38.5	77.5
T1W								
Mean	0	0.810	≤530.680	100.0	66.7	93.3	100.0	94.1
SD	0	0.762	≤21.820	85.7	66.7	92.3	50	82.4
SD	2	0.857	≤32.760	64.3	100.0	100.0	37.5	70.6
SD	3	0.827	≤67.470	85.7	83.3	96	55.6	85.3
SD	5	0.768	≤57.380	60.7	100.0	100.0	35.3	67.6
SD	6	0.780	≤61.780	64.3	100.0	100.0	37.5	70.6
MPP	0	0.810	≤530.680	100.0	66.7	93.3	100.0	94.1

(Continued)

Table 6. (Continued)

MPP	2	0.875*	≤37.570	78.6	83.3	95.7	45.5	79.4
MPP	3	0.786	≤32.740	53.6	100.0	100.0	31.6	61.8
MPP	5	0.762	≤57.530	64.3	83.3	94.7	33.3	67.6
MPP	6	0.792	≤112.920	89.3	66.7	92.6	57.1	85.3
Corticomedullary phase								
Mean	0	0.913*	≤513.190	87.0	83.3	95.2	62.5	86.2
Mean	4	0.812	≤179.350	91.3	66.7	91.3	66.7	86.2
Mean	5	0.826	≤305.720	95.7	66.7	91.7	80.0	89.7
Mean	6	0.848	≤379.660	95.7	66.7	91.7	80.0	89.7
SD	2	0.841	≤181.730	100.0	66.7	92	100	93.1
SD	3	0.862	≤182.440	91.3	83.3	95.5	71.4	89.7
SD	4	0.862	≤208.810	87.0	83.3	95.2	62.5	86.2
SD	5	0.87	≤243.050	95.7	66.7	91.7	80.0	89.7
SD	6	0.841	≤343.660	100.0	66.7	92	100.0	93.1
MPP	0	0.913	≤513.190	87.0	83.3	95.2	62.5	86.2
MPP	2	0.833	≤167.490	100.0	66.7	92	100.0	93.1
MPP	3	0.862	≤154.950	91.3	83.3	95.5	71.4	89.7
MPP	4	0.87	≤194.990	91.3	83.3	95.5	71.4	89.7
MPP	5	0.87	≤254.550	91.3	83.3	95.5	71.4	89.7
MPP	6	0.877	≤321.860	91.3	83.3	95.5	71.4	89.7
Skewness	2	0.826	≤0.450	95.7	83.3	95.7	83.3	93.1
Skewness	3	0.862	≤0.620	82.6	83.3	95.0	55.6	82.8
Kurtosis	2	0.768	≤0.160	47.8	100.0	100.0	33.3	58.6
Nephrographic phase								
Mean	0	0.868*	≤852.020	100.0	66.7	92.3	100.0	93.3
Mean	6	0.778	≤409.880	100.0	50.0	88.9	100.0	90.0
SD	2	0.806	≤167.550	95.8	66.7	92.0	80.0	90.0
SD	3	0.778	≤147.230	75.0	83.3	94.7	45.5	76.7
SD	4	0.799	≤170.910	75.0	83.3	94.7	45.5	76.7
SD	5	0.813	≤180.540	70.8	83.3	94.4	41.7	73.3
SD	6	0.771	≤280.850	100.0	50.0	88.9	100.0	90.0
MPP	0	0.868	≤852.020	100.0	66.7	92.3	100.0	93.3
MPP	2	0.771	≤112.770	75.0	83.3	94.7	45.5	76.7
MPP	4	0.771	≤261.790	95.8	66.7	92.0	80.0	90.0

significant overlap with RCC was frequently observed.[38,39] Tumors with organoid histology have been observed to show intense arterial enhancement higher than RCC and venous washout, whereas those with tubulocystic histology showed slow, gradual enhancement.[5]

Our study had a few limitations. First, the RCC group had a skewed distribution with predominance of clear cell RCC. Hence, the TA findings would be more representative of this subtype than papillary or chromophobe RCC. In the case of lpAML and oncocytoma, up to four lesions were selected per patient. Since the absolute number of patients with these two entities was small, this would bring significant cluster effect which was unaccounted for. Third, only first-order texture parameters were assessed in our study. Although the use of higher order statistical parameters would have provided more parameters for assessment, the huge volume of data generated would make analysis more computationally intensive and of questionable value, especially since the biological basis for several of these parameters is yet unknown. Finally, machine-learning techniques could have enabled the generation of a combination of texture parameters in

Table 7. Sequence-wise best-performing parameters (having AUC of at least 0.8) in the differentiation of RCC from onco-cytoma

Sequence	Parameter	SSF value	AUC
T2W	MPP	6	0.814
DWI b500	MPP	6	0.931
DWI b1000	Mean	0	0.935
ADC map	SD	0	0.875
T1W	MPP	2	0.875
Corticomedullary phase	Mean	0	0.913
Nephrographic phase	Mean	0	0.868

better classifying the tumors. However, we could not apply machine-learning techniques due to our small sample size. Finally, we did not assess interobserver agreement for the measured texture parameters.

In conclusion, MRTA-generated several parameters which showed excellent diagnostic performance (AUC > 0.8) in the differentiation of RCC from lpAML and oncocytoma. In the future, once more uniform acquisition protocols are implemented to ensure reproducibility, it could serve as a useful, quantitative imaging tool in the differentiation of the above pathologies. However, as of now, histopathology continues to be the gold standard and larger validation studies would be needed before MRTA can be used in routine practice.

REFERENCES

1. Bauman TM, Potretzke AM, Wright AJ, Knight BA, Vetter JM, Figenshau RS. Partial nephrectomy for presumed renal-cell carcinoma: incidence, predictors, and perioperative outcomes of benign lesions. *J Endourol* 2017; **31**: 412–7. doi: https://doi.org/10.1089/end.2016.0667

2. Yang C-W, Shen S-H, Chang Y-H, Chung H-J, Wang J-H, Lin ATL, et al. Are there useful CT features to differentiate renal cell carcinoma from lipid-poor renal angiomyolipoma? *AJR Am J Roentgenol* 2013; **201**: 1017–28. doi: https://doi.org/10.2214/AJR.12.10204

3. Jinzaki M, Silverman SG, Akita H, Nagashima Y, Mikami S, Oya M. Renal angiomyolipoma: a radiological classification and update on recent developments in diagnosis and management. *Abdom Imaging* 2014; **39**: 588–604. doi: https://doi.org/10.1007/s00261-014-0083-3

4. Silverman SG, Gan YU, Mortele KJ, Tuncali K, Cibas ES. Renal masses in the adult patient: the role of percutaneous biopsy. *Radiology* 2006; **240**: 6–22. doi: https://doi.org/10.1148/radiol.2401050061

5. Ishigami K, Jones AR, Dahmoush L, Leite LV, Pakalniskis MG, Barloon TJ. Imaging spectrum of renal oncocytomas: a pictorial review with pathologic correlation. *Insights Imaging* 2015; **6**: 53–64. doi: https://doi.org/10.1007/s13244-014-0373-x

6. Rosenkrantz AB, Hindman N, Fitzgerald EF, Niver BE, Melamed J, Babb JS. Mri features of renal oncocytoma and chromophobe renal cell carcinoma. *AJR Am J Roentgenol* 2010; **195**: W421–7. doi: https://doi.org/10.2214/AJR.10.4718

7. Lubner MG, Smith AD, Sandrasegaran K, Sahani DV, Pickhardt PJ. Ct texture analysis: definitions, applications, biologic correlates, and challenges. *Radiographics* 2017; **37**: 1483–503. doi: https://doi.org/10.1148/rg.2017170056

8. Coy H, Hsieh K, Wu W, Nagarajan MB, Young JR, Douek ML, et al. Deep learning and radiomics: the utility of Google TensorFlow™ inception in classifying clear cell renal cell carcinoma and oncocytoma on multiphasic CT. *Abdom Radiol* 2019; **44**: 2009–20. doi: https://doi.org/10.1007/s00261-019-01929-0

9. Deng Y, Soule E, Cui E, Samuel A, Shah S, Lall C, et al. Usefulness of CT texture analysis in differentiating benign and malignant renal tumours. *Clin Radiol* 2020; **75**: 108–15. doi: https://doi.org/10.1016/j.crad.2019.09.131

10. Feng Z, Rong P, Cao P, Zhou Q, Zhu W, Yan Z, et al. Machine learning-based quantitative texture analysis of CT images of small renal masses: differentiation of angiomyolipoma without visible fat from renal cell carcinoma. *Eur Radiol* 2018; **28**: 1625–33. doi: https://doi.org/10.1007/s00330-017-5118-z

11. Hodgdon T, McInnes MDF, Schieda N, Flood TA, Lamb L, Thornhill RE. Can quantitative CT texture analysis be used to differentiate Fat-poor renal angiomyolipoma from renal cell carcinoma on unenhanced CT images? *Radiology* 2015; **276**: 787–96. doi: https://doi.org/10.1148/radiol.2015142215

12. Lee HS, Hong H, Jung DC, Park S, Kim J. Differentiation of fat-poor angiomyolipoma from clear cell renal cell carcinoma in contrast-enhanced MDCT images using quantitative feature classification. *Med Phys* 2017; **44**: 3604–14. doi: https://doi.org/10.1002/mp.12258

13. Li Y, Huang X, Xia Y, Long L. Value of radiomics in differential diagnosis of chromophobe renal cell carcinoma and renal oncocytoma. *Abdom Radiol* 2019;29 Oct 2019. doi: https://doi.org/10.1007/s00261-019-02269-9

14. Nie P, Yang G, Wang Z, Yan L, Miao W, Hao D, et al. A CT-based radiomics nomogram for differentiation of renal angiomyolipoma without visible fat from homogeneous clear cell renal cell carcinoma. *Eur Radiol* 2020; **30**: 1274–84. doi: https://doi.org/10.1007/s00330-019-06427-x

15. Sasaguri K, Takahashi N, Gomez-Cardona D, Leng S, Schmit GD, Carter RE, et al. Small (< 4 cm) Renal Mass: Differentiation of Oncocytoma From Renal Cell Carcinoma on Biphasic Contrast-Enhanced CT. *AJR Am J Roentgenol* 2015; **205**: 999–1007. doi: https://doi.org/10.2214/AJR.14.13966

16. Sun X-Y, Feng Q-X, Xu X, Zhang J, Zhu F-P, Yang Y-H, et al. Radiologic-Radiomic machine learning models for differentiation of benign and malignant solid renal masses: comparison with Expert-Level radiologists. *AJR Am J Roentgenol* 2020; **214**: W44–54. doi: https://doi.org/10.2214/AJR.19.21617

17. Tang Z, Yu D, Ni T, Zhao T, Jin Y, Dong E. Quantitative analysis of multiphase contrast-enhanced CT images: a pilot study of preoperative prediction of Fat-Poor angiomyolipoma and renal cell carcinoma. *AJR Am J Roentgenol* 2019;: 1–13.

18. Varghese BA, Chen F, Hwang DH, Cen SY, Desai B, Gill IS, et al. Differentiation of predominantly solid enhancing lipid-poor renal cell masses by use of contrast-enhanced CT: evaluating the role of texture in tumor subtyping. *AJR Am J Roentgenol* 2018; **211**: W288–96. doi: https://doi.org/10.2214/AJR.18.19551

19. Yan L, Liu Z, Wang G, Huang Y, Liu Y, Yu Y, et al. Angiomyolipoma with minimal fat: differentiation from clear cell renal cell carcinoma and papillary renal cell carcinoma by texture analysis on CT images. *Acad Radiol* 2015; **22**: 1115–21. doi: https://doi.org/10.1016/j.acra.2015.04.004

20. Yang G, Gong A, Nie P, Yan L, Miao W, Zhao Y, et al. Contrast-Enhanced CT texture analysis for distinguishing Fat-Poor renal angiomyolipoma from chromophobe renal

cell carcinoma. *Mol Imaging* 2019; **18**: 1536012119883161. doi: https://doi.org/10.1177/1536012119883161

21. Yang R, Wu J, Sun L, Lai S, Xu Y, Liu X, et al. Radiomics of small renal masses on multiphasic CT: accuracy of machine learning-based classification models for the differentiation of renal cell carcinoma and angiomyolipoma without visible fat. *Eur Radiol* 2020; **30**: 1254-1263. doi: https://doi.org/10.1007/s00330-019-06384-5

22. You M-W, Kim N, Choi HJ. The value of quantitative CT texture analysis in differentiation of angiomyolipoma without visible fat from clear cell renal cell carcinoma on four-phase contrast-enhanced CT images. *Clin Radiol* 2019; **74**: 547–54. doi: https://doi.org/10.1016/j.crad.2019.02.018

23. Yu H, Scalera J, Khalid M, Touret A-S, Bloch N, Li B, et al. Texture analysis as a radiomic marker for differentiating renal tumors. *Abdom Radiol* 2017; **42**: 2470–8. doi: https://doi.org/10.1007/s00261-017-1144-1

24. Li H, Li A, Zhu H, Hu Y, Li J, Xia L, et al. Whole-Tumor quantitative apparent diffusion coefficient histogram and texture analysis to differentiation of minimal fat angiomyolipoma from clear cell renal cell carcinoma. *Acad Radiol*(eds 2019; **26**: 632–9. doi: https://doi.org/10.1016/j.acra.2018.06.015

25. Goyal A, Razik A, Kandasamy D, Seth A, Das P, Ganeshan B, et al. Role of Mr texture analysis in histological subtyping and grading of renal cell carcinoma: a preliminary study. *Abdom Radiol* 2019; **44**: 3336–49.

26. Park JJ, Kim CK. Small (< 4 cm) Renal Tumors With Predominantly Low Signal Intensity on T2-Weighted Images: Differentiation of Minimal-Fat Angiomyolipoma From Renal Cell Carcinoma. *AJR Am J Roentgenol* 2017; **208**:

124–30. doi: https://doi.org/10.2214/AJR.16.16102

27. Miles KA, Ganeshan B, Hayball MP. Ct texture analysis using the filtration-histogram method: what do the measurements mean? *Cancer Imaging* 2013; **13**: 400–6.

28. Hindman N, Ngo L, Genega EM, Melamed J, Wei J, Braza JM, et al. Angiomyolipoma with minimal fat: can it be differentiated from clear cell renal cell carcinoma by using standard Mr techniques? *Radiology* 2012; **265**: 468–77. doi: https://doi.org/10.1148/radiol.12112087

29. Ding Y, Zeng M, Rao S, Chen C, Fu C, Zhou J. Comparison of biexponential and Monoexponential model of diffusion-weighted imaging for distinguishing between common renal cell carcinoma and fat poor angiomyolipoma. *Korean J Radiol* 2016; **17**: 853–63. doi: https://doi.org/10.3348/kjr.2016.17.6.853

30. Taouli B, Thakur RK, Mannelli L, Babb JS, Kim S, Hecht EM, et al. Renal lesions: characterization with diffusion-weighted imaging versus contrast-enhanced MR imaging. *Radiology* 2009; **251**: 398–407. doi: https://doi.org/10.1148/radiol.2512080880

31. Tanaka H, Yoshida S, Fujii Y, Ishii C, Tanaka H, Koga F, et al. Diffusion-Weighted magnetic resonance imaging in the differentiation of angiomyolipoma with minimal fat from clear cell renal cell carcinoma. *Int J Urol* 2011; **18**: 727–30. doi: https://doi.org/10.1111/j.1442-2042.2011.02824.x

32. Park BK. Renal angiomyolipoma: radiologic classification and imaging features according to the amount of fat. *AJR Am J Roentgenol* 2017; **209**: 826–35. doi: https://doi.org/10.2214/AJR.17.17973

33. Sasiwimonphan K, Takahashi N, Leibovich BC, Carter RE, Atwell TD, Kawashima

A, Small KA. Small (<4 cm) renal mass: differentiation of angiomyolipoma without visible fat from renal cell carcinoma utilizing MR imaging.. *Radiology* 2012; **263**: 160–8. doi: https://doi.org/10.1148/radiol.12111205

34. Scialpi M, Di Maggio A, Midiri M, Loperfido A, Angelelli G, Rotondo A. Small renal masses: assessment of lesion characterization and vascularity on dynamic contrast-enhanced MR imaging with fat suppression. *AJR Am J Roentgenol* 2000; **175**: 751–7. doi: https://doi.org/10.2214/ajr.175.3.1750751

35. Akın IB, Altay C, Güler E, Çamlıdağ İlkay, Harman M, Danacı M, et al. Discrimination of oncocytoma and chromophobe renal cell carcinoma using MRI. *Diagn Interv Radiol* 2019; **25**: 5–13. doi: https://doi.org/10.5152/dir.2018.18013

36. Galmiche C, Bernhard J-C, Yacoub M, Ravaud A, Grenier N, Cornelis F. Is multiparametric MRI useful for differentiating oncocytomas from chromophobe renal cell carcinomas? *AJR Am J Roentgenol* 2017; **208**: 343–50. doi: https://doi.org/10.2214/AJR.16.16832

37. Hötker AM, Mazaheri Y, Wibmer A, Zheng J, Moskowitz CS, Tickoo SK, et al. Use of DWI in the differentiation of renal cortical tumors. *AJR Am J Roentgenol* 2016; **206**: 100–5. doi: https://doi.org/10.2214/AJR.14.13923

38. Young JR, Margolis D, Sauk S, Pantuck AJ, Sayre J, Raman SS. Clear cell renal cell carcinoma: discrimination from other renal cell carcinoma subtypes and oncocytoma at multiphasic multidetector CT. *Radiology* 2013; **267**: 444–53. doi: https://doi.org/10.1148/radiol.13112617

39. Bird VG, Kanagarajah P, Morillo G, Caruso DJ, Ayyathurai R, Leveillee R, et al. Differentiation of oncocytoma and renal cell carcinoma in small renal masses. *World J Urol* 2011; **29**: 787–92.